Supplementary Information: Coherent Control of a Long-Lived Nuclear Memory Spin in a Germanium Vacancy Multi-Qubit Node

Nick Grimm,[1,*] Katharina Senkalla,[1,*] Philipp J. Vetter,[1,*] Jurek Frey,[2,3] Prithvi Gundlapalli,[1] Tommaso Calarco,[4,5,6] Genko Genov,[1] Matthias M. Müller,[4] and Fedor Jelezko[1]

[1] *Institute for Quantum Optics, Ulm University, Albert-Einstein-Allee 11, 89081 Ulm, Germany*
[2] *Peter Grünberg Institute-Quantum Computing Analytics (PGI-12), Forschungszentrum Jülich GmbH, D-52425 Jülich, Germany*
[3] *Theoretical Physics, Saarland University, D-66123 Saarbrücken, Germany*
[4] *Peter Grünberg Institute-Quantum Control (PGI-8), Forschungszentrum Jülich GmbH, D-52425 Jülich, Germany*
[5] *Institute for Theoretical Physics, University of Cologne, D-50937 Germany*
[6] *Dipartimento di Fisica e Astronomia, Università di Bologna, 40127 Bologna, Italy*

(Dated: January 14, 2025)

CONTENTS

Sample and setup description 1

Electron spin initialization and lifetime 1

Hyperfine coupling parameter estimation 2
Further error analysis 3

Nuclear spin pumping 3

Driving field optimization with QuOCS 4

Further details on ^{13}C spin coherence experiments 4

Numerical simulation and estimation of the memory time limit 5
Heating estimation 8

References 9

SAMPLE AND SETUP DESCRIPTION

We work with a ⟨111⟩-oriented diamond, that was grown under high pressure high temperature (HPHT) conditions, during which Ge is naturally incorporated and formed GeV centers without additional annealing [1]. The investigated GeV center is located in a solid immersion lens (SIL) of 10 µm diameter and microwave (mw) and radio frequency (rf) fields are applied through a 20 µm-thick copper wire spanned over the diamonds surface nearby the SIL.

A detailed setup description can be found in the supplementary of [2]. We state here most important details and changes compared to previous configuration. Experiments are performed in a dilution refrigerator (Bluefors, BF-LD400) with optical access for a home-built confocal microscope. A superconducting vector magnet from American Magnetics, Inc. allows to precisely align the magnetic field with the GeV by optimizing electron spin lifetime at 4 K, yielding $T_{1,e}^{4\mathrm{K}} = (3.41 \pm 0.20)$ ms. As we observe a small decay of the magnetic field (∼4.7 µT/h) in the persistent mode, we operate the magnet actively stabilized with magnetic field fluctuations of $std = 0.05$ G. For resonant excitation we use a Sirah Lasertechnik Matisse 2 DS single frequency tunable dye laser at 602 nm (Rhodamin 6G in ethylene glycol). Pulsed optical excitation is realized by using a double-path acousto optical modulator (AOM) configuration for which the distorted optical mode is cleaned by a single mode polarization maintaining patch cord fiber PM-S405-XP from Thorlabs. For in- and outcoupling we use a mounted aspheric lens form Thorlabs (A260TM-A). After the outcoupler we use a 605/20 clean up filter and adjust the beam size to fill the back aperture of the Newport objective (Li-60X with NA of 0.85). For mw and rf manipulation we use the positive and negative output of the same channel of the AWG (Tektronix 70000B HP). The designated mw channel is filtered by a high- and low pass filter and pulses are amplified by an amplifier (ar 50S1G6). Similarly, the designated rf channel is filtered by a DC block and low pass filter before the pulses are amplified by a second amplifier (ar 125A400). The mw and rf lines are then combined by a diplexer (Procom PRO-DIPX225/330) and provided to the cryostat.

ELECTRON SPIN INITIALIZATION AND LIFETIME

Figure S.1(a) shows the fluorescence time trace of a 5.5 ms long laser pulse resonant to c_1, applied to an initially prepared $|\downarrow_e\rangle$ state, from which we determine an initialization fidelity of 98 %. The fidelity is calculated according to $1 - \frac{a}{h}$, where h and a are values of the exponential fit at 0 ms and 5.5 ms, respectively. For the electron spin lifetime we measure $T_{1,e} = (20.7 \pm 2.0)$ s, as

* These authors contributed equally to this work.
Corresponding author: katharina.senkalla@uni-ulm.de

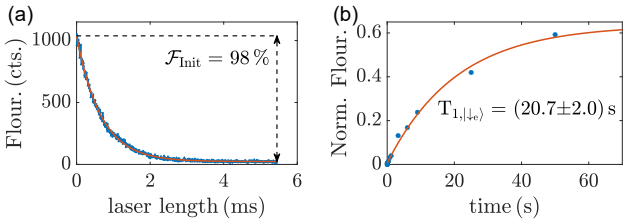

FIG. S.1. Electron spin properties. (a) Exemplary initialization curve for the $|\uparrow_e\rangle$ state using a 5.5 ms laser at optical transition c_1. (b) $T_{1,e}$ measurement in the $|\downarrow_e\rangle$ state.

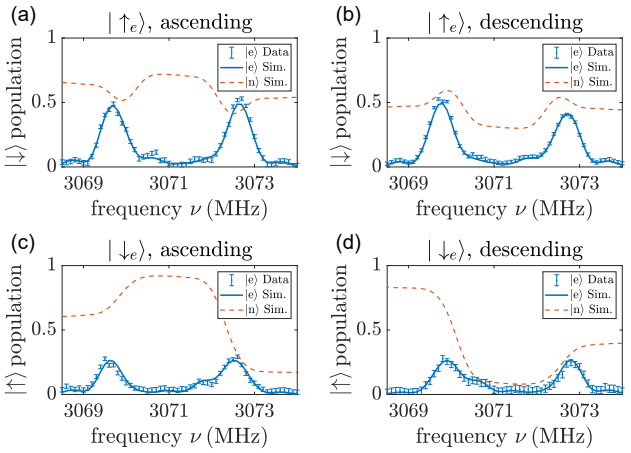

FIG. S.2. Pulsed ODMR measurements with simulation results. The fit is performed for four different experiments: (a) electron spin $|\uparrow_e\rangle$ with ascending frequency sweep direction, (b) electron spin $|\uparrow_e\rangle$ with descending frequency sweep direction, (c) electron spin $|\downarrow_e\rangle$ with ascending frequency sweep direction and (d) electron spin $|\downarrow_e\rangle$ with descending frequency sweep direction. The orange dotted line shows the nuclear spin population before the microwave pulse.

shown in Fig. S.1 (b).

HYPERFINE COUPLING PARAMETER ESTIMATION

We perform four pulsed ODMR measurements, which are shown in Fig. S.2 (a) - (d) with their corresponding fit. The four spectra differ by the frequency sweep direction and to which state the electron spin is re-initialized via the laser pulse. Each spectrum is normalized by a Rabi experiment that is performed after each run of the sequence (see Fig. S.7 (a) for details). The obtained measurement data corresponds to the average fluorescence signal of around 3470 repetitions of the measurement sequence (pulsed ODMR + Rabi).

To extract the hyperfine coupling parameters A_{zx} and A_{zz} between the electron and nuclear spin, we numerically simulate the obtained spectra according to the Hamiltonian Eq. (1) from the main text.

The initial nuclear spin state $\rho_i^n = p_i\,|\uparrow_n\rangle\langle\uparrow_n| + (1-p_i)\,|\downarrow_n\rangle\langle\downarrow_n|$ is left open as a fit parameter since the measured spectra reflect the averaged fluorescence signal, and the nuclear spin can become polarized through the ODMR measurements and subsequent Rabi experiment. The states $|\uparrow_n\rangle$ and $|\downarrow_n\rangle$ refer to the nuclear spin states for the diagonalized Hamiltonian along the corresponding quantization axis for a given electron spin state. The nuclear spin is then initalized along the corresponding quantization axis.

Considering the low temperature and the resulting long nuclear spin population lifetimes, we model the laser pulse as a Kraus operator of a depolarizing channel [3], fully re-initializing the electron spin to either $|\uparrow_e\rangle$ or $|\downarrow_e\rangle$, while leaving the nuclear spin untouched. To account for the laser length of 5.5 ms and the averaging over thousands of repetitions, we let the nuclear spin fully dephase through a randomized detuning.

Given the custom sample holder, the diamond is unlikely to be perfectly placed in the center of the magnetic field generated by the vector magnet. The objective and other hardware components in the sample chamber may also cause slight deviation of the set magnetic field amplitude. To account for those effects, the strength of the magnetic field B_i is treated as a fit parameter that can differ for each of the four spectra. B_i is then used to construct the hyperfine coupling parameters A_{zx} and A_{zz} according to Eq. (2) and Eq. (3) from the main text. The nuclear transition frequencies $\omega_{\mathrm{rf2}} = (2\pi)\,(493.62\pm0.04)\,\mathrm{kHz}$ and $\omega_{\mathrm{rf1}} = (2\pi)\,(2489.73\pm0.06)\,\mathrm{kHz}$, required for this calculation, are extracted from the nuclear Ramsey fringes shown in Fig. S.7 (b) and in Fig. 2 (d) in the main text.

The detuning of Eq. (1) in the main text is given by $\Delta_{i,k} = \gamma_e^{\mathrm{eff}} B_i - (2\pi)\nu_k$, where the subscript k is an index for the current measurement step, and $i = (a), (b), (c), (d)$ denotes that the magnetic field B_i might vary in each experiment in Fig. S.2(a,b,c,d). Thus the detuning depends on both, the frequency step ν_k and the magnetic field B_i from the particular ODMR sequence. While the magnetic field B_i varies between the four different ODMR spectra but is kept during one sequence, the gyromagnetic ratio γ_e^{eff} is a shared property among all spectra. Hereby, γ_e^{eff} denotes the effective gyromagnetic ratio, which includes both, the electron Zeeman effect and the quenched orbital Zeeman effect. While the gyromagnetic ratio of a free electron spin is well known, the orbital contribution of the GeV has not been experimentally determined yet [4]. For this reason we combine both in the fit parameter γ_e^{eff}.

We include the electron spin dephasing ($T_{2,e}^* = 1.43\,\mu\mathrm{s}$ [2]) during the microwave π-pulse by a randomized constant detuning with a standard deviation of $\sigma_\delta \approx \sqrt{2}/T_{2,e}^* = 2\pi \cdot 146$ kHz [2] and a mean of 0. Each simulated spectrum is then averaged over 2500 iterations. We use differential evolution [5] to find the set of parameters, i.e. the gyromagnetic ratio γ_e^{eff}, the magnetic field B_i, and the initial nuclear spin population p_i, that minimizes the sum of the squared differences between the measured and simulated spectra. These parameters are

then used as starting points in a final fit via the least-square method, that is individually performed for the four ODMR measurements while keeping the product $\gamma_e^{\text{eff}} B_i$ constant. Our simulation fits the data very well. We obtain an R^2 of 0.9854 for $|\uparrow_e\rangle$ and 0.9328 for $|\downarrow_e\rangle$ with an ascending frequency sweep direction and 0.9854 for $|\uparrow_e\rangle$ and 0.9568 for $|\downarrow_e\rangle$ with a descending frequency sweep direction. This leads to the following parameters, where the subscript describes the electron spin manifold and the superscript the ODMR sweep direction:

- $\gamma_{|\uparrow_e\rangle}^{ascending} = (2\pi)\, 31.6162165179458\, \frac{\text{GHz}}{\text{T}}$,
- $\gamma_{|\downarrow_e\rangle}^{ascending} = (2\pi)\, 31.6165307831433\, \frac{\text{GHz}}{\text{T}}$,
- $\gamma_{|\uparrow_e\rangle}^{descending} = (2\pi)\, 31.6135603066038\, \frac{\text{GHz}}{\text{T}}$,
- $\gamma_{|\downarrow_e\rangle}^{descending} = (2\pi)\, 31.6147971633278\, \frac{\text{GHz}}{\text{T}}$,
- $B_{|\uparrow_e\rangle}^{ascending} = 97.140\,\text{mT} \pm 0.004\,\text{mT}$,
- $B_{|\downarrow_e\rangle}^{ascending} = 97.138\,\text{mT} \pm 0.006\,\text{mT}$,
- $B_{|\uparrow_e\rangle}^{descending} = 97.149\,\text{mT} \pm 0.004\,\text{mT}$,
- $B_{|\downarrow_e\rangle}^{descending} = 97.146\,\text{mT} \pm 0.005\,\text{mT}$,
- $p_{|\uparrow_e\rangle}^{ascending} = 0.34508 \pm 0.00004$,
- $p_{|\downarrow_e\rangle}^{ascending} = 0.60563 \pm 0.00007$,
- $p_{|\uparrow_e\rangle}^{descending} = 0.55639 \pm 0.00005$,
- $p_{|\downarrow_e\rangle}^{descending} = 0.39752 \pm 0.00007$.

According to Eq. (2) and Eq. (3) from the main text we then obtain the mean values $A_{zx} = 2\pi\,(602.81 \pm 0.27)$ kHz and $A_{zz} = 2\pi\,(2862.34 \pm 0.14)$ kHz for the hyperfine coupling parameters.

Further error analysis

While only the magnetic fields B_i go into the calculation of the hyperfine coupling parameters, γ_e^{eff} and B_i are coupled through the detuning $\Delta_i = \gamma_e^{\text{eff}} B_i - (2\pi)\nu$. For this reason we kept the product $\gamma_e^{\text{eff}} B_i$ fixed while performing the final fit after the differential evolution. To better understand the parameter landscape and the associated fit error, we sweep γ_e^{eff} and B_i in the range of $[30.712\,\frac{\text{GHz}}{\text{T}}, 32.328\,\frac{\text{GHz}}{\text{T}}]$ and $[95\,\text{mT}, 100\,\text{mT}]$ for each of the four ODMR measurements and calculate the resulting R^2 value, as shown in Fig. S.3 (a) - (d). For each of the four plots we select the highest R^2 for all γ_e^{eff} and visualize the mean value in Fig. S.3 (e). We observe a smooth parameter landscape with a distinct maximum. We can thus conclude that our model accurately represents the experiment, and our fit results are precise, as the fit avoids being trapped in local maxima.

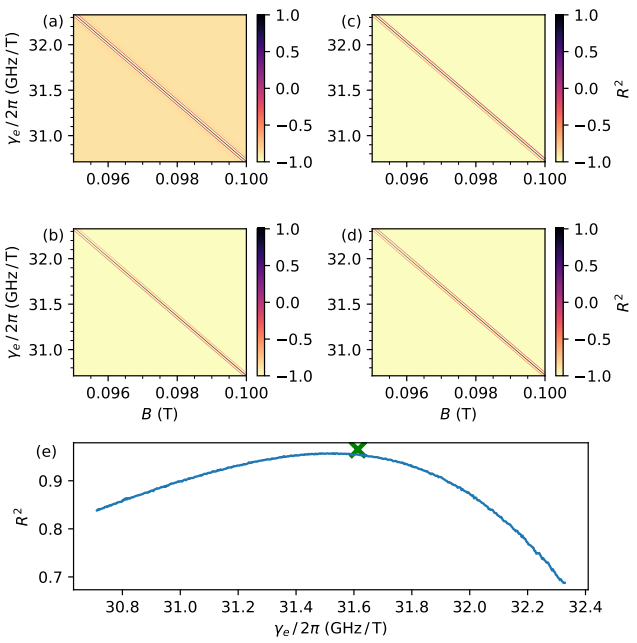

FIG. S.3. R^2 of the model for different values of γ_e^{eff} and B_i. The images differ by their electron spin state of $|\uparrow_e\rangle$ for (a) ascending frequency sweep direction, (b) for descending frequency sweep direction and $|\downarrow_e\rangle$ for (c) ascending frequency sweep direction and (d) for descending frequency sweep direction. (e) Mean R^2 of the highest individually achieved R^2 of all four ODMR measurements for the respective γ_e^{eff}. The cross indicates the best mean R^2 value achieved in the simulation which is slightly higher than the mean R^2 values in the sweep due to the finite sampling size of the sweep.

NUCLEAR SPIN PUMPING

Due to the strong hyperfine interaction, we already observe in the pulsed ODMR measurements that the nuclear spin can be polarized through the repetitive application of mw and laser pulses. We can exploit this effect to implement a spin pumping scheme for initialization of the ^{13}C nuclear spin. As illustrated in Fig. 1 (b) in the main text, the nuclear spin experiences a different quantization axis depending on the state of the electron spin. In our system, due to the large A_{zx} and a $A_{zz}/2$ that is in the order of the bare nuclear Larmor frequency the angle between the quantization axes is significant ($\sim 30°$). As a result, the simultaneous flip of the electron and nucleus, which is typically forbidden, becomes partially allowed [6]. Now, to achieve polarization built-up, a spin pumping scheme has to meet two criteria. First, considering the two hyperfine levels in an electron spin subspace, we need to be able to selectively depopulate one level while leaving the other untouched. In the remainder of this paragraph we will refer to the untouched level as dark state. Due to the large energy gap ω_{rf1} this condition is well fulfilled in the $|\downarrow_e\rangle$ manifold, and choosing a narrow-band mw π-pulse at mw1 or mw2 can selectively depopulate one of the levels. On

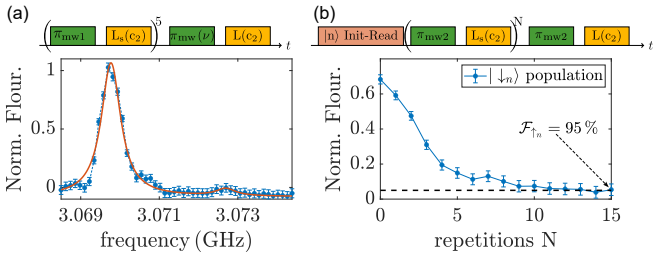

FIG. S.4. Nuclear spin initialization via spin pumping. (a) Nuclear spin pumping scheme using repetitive π mw pulse and laser elements to initialize the nuclear spin probed with a pulsed ODMR. (b) Pulse sequence and experiment to estimate the initialization fidelity of the nuclear spin after N repetitions using the spin pumping scheme. The population of the nuclear spin is prepared with the projection-SWAP gate.

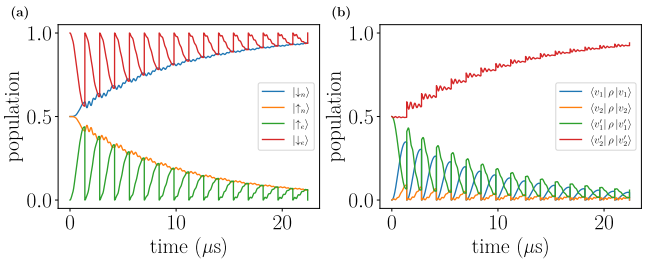

FIG. S.5. Nuclear spin initialization with electron resets (Simulation). The simulated fidelity for $N = 15$ is 94%, which is close to the experimental results. (a) The dynamics of the system if we trace out the other respective spin. (b) Dynamics in the eigenbasis within the $|\downarrow_e\rangle$ sub-manifold, with v_i denoting the eigenvectors (see following section for definition).

the other hand, the small energy gap ω_{rf2} and the limited linewidth resolution, $\propto 1/(\pi T^*_{2,e})$ [7], prohibits the formation of an efficient dark state in the $|\uparrow_e\rangle$ manifold. Second, we need a decay rate to the dark state. For us, the laser leads to an electron reset causing a change of the quantization axis of the nuclear spin. This creates a decay channel to the dark state while we pump the other state empty.

Hence, for the spin pumping scheme to work we start by preparing the electron spin in the $|\downarrow_e\rangle$ state with a 5.5 ms laser pulse at c_2. After application of a π-pulse on the mw1 or mw2 transition, we re-initialize the electron spin and repeat this process N times. In Fig. S.4 (a) the spin pumping scheme ($N = 5$ repetitions) is probed with a pulsed ODMR experiment showing almost no population present in the $|\uparrow_n\rangle$ state. However, due to the change in nuclear spin polarization throughout the ODMR measurement, we cannot determine the initialization fidelity with the ODMR measurement after a specific number of repetitions N. Thus, we equally prepare the initial nuclear spin state for every point with the projection-SWAP in Fig. S.4 (b). This allows us to estimate an initialization fidelity of the nuclear spin using the spin pumping scheme of 95 % after repeating the sequence $N = 15$ times (mw π pulse duration 1.4 μs). Numeric simulations displayed in Fig. S.5, accounting for electron spin dephasing, show that we can reach up to 98.7 % polarization of the nuclear spin by repeating this 50 times, with the same π mw pulse duration of 1.4 µs as in the experiment.

DRIVING FIELD OPTIMIZATION WITH QUOCS

With the fitted Hamiltonian parameters, we can optimize the driving field to implement an operation of our choice. The corresponding Hamiltonian (in the rotating frame at the driving field frequency after using the rotating wave approximation) can be written as

$$H_d = \Omega_e(t)\left[\cos\phi(t)S_x + \sin\phi(t)S_y\right] \tag{1}$$

where $\Omega_e(t)$ is the time-dependent Rabi frequency and $\phi(t)$ is its time-dependent phase. The driving frequency is chosen to be $\omega_d = \omega_{\mathrm{mw2}} + \omega_{\mathrm{rf1}}$.

With optimal control, we can now design functions which implement a population transfer procedure. Because the nuclear spin eigenstate depends on the electron state, we choose to polarize along the quantization axis defined by the electron spin being in $|\downarrow_e\rangle$

$$\mathrm{FoM} = 1 - \langle v_2|\,\rho\,|v_2\rangle - \langle v_2'|\,\rho\,|v_2'\rangle \tag{2}$$

where $v_2(v_1)$ is the eigenvector corresponding to $|\downarrow_e\uparrow_n\rangle$ ($|\downarrow_e\downarrow_n\rangle$). We introduced here $v_i' = (\sigma_x \otimes \mathbf{1})v_i$, which point for the nucleus subspace in the same direction as the eigenvectors in the $|\downarrow_e\rangle$-subspace but have a flipped electron spin state. We minimize the FoM using the QuOCS-Software [8] by optimizing $\Omega_e(t)$ and $\phi(t)$ with the dCRAB-algorithm [9, 10].

We restrict our search space to functions in the Fourier-basis domain, limit the maximal Rabi-frequency and ensure with a flattop Gaussian envelope (raise time of 100 ns) that we do not have sudden jumps in the driving amplitude.

We then start the optimization (settings for dCRAB: 10 super iterations, 1000 function evaluations per super iteration) for different evolution times τ. The optimization process and its results are discussed in Figure S.6. According to the simulations, an efficient population transfer with high fidelity can be realized, achieving a minimum average nuclear polarization of 99.9%, without necessitating electron reinitialization.

FURTHER DETAILS ON ^{13}C SPIN COHERENCE EXPERIMENTS

As shown in the main text, we initialize and readout the nuclear spin by a projection-SWAP gate used for population transfer. Depending on the electron spin state we use a different mw and laser transition for the sequence in Fig. 2 (a) of the main text. Here, the subscript s (si-

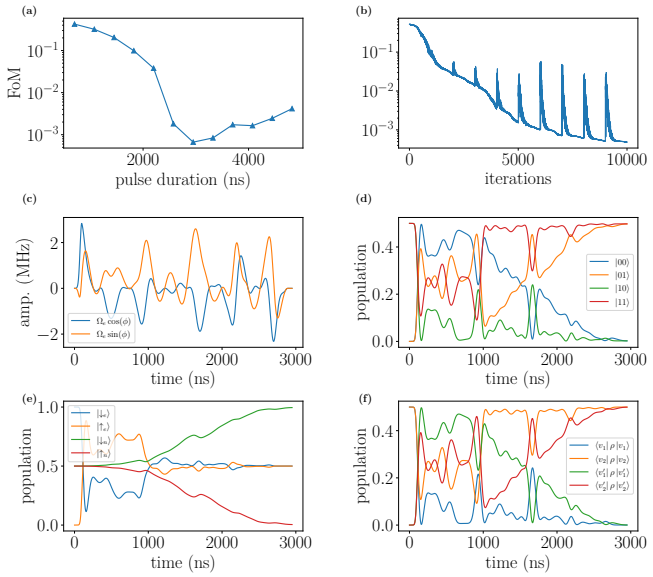

FIG. S.6. Optimization process for the initialization of the nuclear spin with a single optimized mw pulse. (a) Resulting polarization infidelity of the nucleus for different pulse durations, where each point was optimized separately (averaged over 5000 OU noise realizations). (b) Optimization progress for a fixed pulse duration (Optimization is done for 100 fixed OU noise realizations). (c) Resulting driving pulse shapes for one optimized duration. (d)-(f) Time evolution (d) computational basis, (e) tracing out the other spin, (f) populations along the nuclear quantization axis defined by $|\downarrow_e\rangle$ during the application of an optimized pulse. (b) - (f) relate to a pulse duration of 2950 ns.

lenced) for a laser element indicates that we do not record data for this laser element.

We initialize our two-qubit system in the respective eigenbasis of our diagonalized Hamiltonian. For $|\downarrow_e\rangle$ we prepare the system in $|\downarrow_e\downarrow_n\rangle$ using a laser at c_2 and π-pulses at mw1 and rf2. For $|\uparrow_e\rangle$ we initialize in $|\uparrow_e\downarrow_n\rangle$ using a laser at c_1 and π-pulses at mw2 and rf2. The corresponding Rabi frequency used for rf2 is $\Omega_{\mathrm{rf2}} = (2\pi)(7.73 \pm 0.05)\,\mathrm{kHz}$ inferring a π rf pulse length of 65 µs. Furthermore, as outlined in the main text, each measurement is followed by an electron Rabi normalization sequence, which includes two successive conditional mw pulses, as depicted in Fig. S.7(a). The maximum and minimum of the sinusodial part of the fit is used to normalize the obtained fluorescence of the respective measurement.

Fig. S.7(b) shows $T^*_{2,\mathrm{rf2}} = (3.35 \pm 0.21)\,\mathrm{ms}$ for the nuclear spin within the $|\uparrow_e\rangle$ manifold. This longer T_2^*, compared to the one shown in the main text for $|\downarrow_e\rangle$, can be partly attributed to magnetic field fluctuations having a lower impact in the $|\uparrow_e\rangle$ state. This can be explained by noting that the contribution of the unperturbed term $(A_{zx}/2)^2$ to $\omega_{\mathrm{rf1,rf2}}$ is greater in the $|\uparrow_e\rangle$ state than in the $|\downarrow_e\rangle$ state. Specifically, in the $|\uparrow_e\rangle$ state, ω^2_{rf2} is given by $(A_{zz}/2 - \gamma_n B)^2 + (A_{zx}/2)^2$, which includes a larger contribution from $(A_{zx}/2)^2$. Further, the variations in the T_2^* values of the ^{13}C could be attributed to slight differences in experimental conditions between the two measurements conducted during separate cooling cycles. However, further investigation is required to fully explain this phenomena.

To investigate the influence of pulse errors on our nuclear spin coherence time we perform a XY8 dynamical decoupling sequence and compare it to the CPMG-8 one. The pulse sequence and the resulting measurement for XY8 are shown in Fig. S.7 (c) and (d), respectively. We obtain $T^{\mathrm{XY8}}_{2,\mathrm{rf1}} = (1.49 \pm 0.10)\,\mathrm{s}$ for XY8, which is comparable to the CPMG-8 result $T^{\mathrm{CPMG8}}_{2,\mathrm{rf1}} = (1.36 \pm 0.14)\,\mathrm{s}$. Additionally, to estimate the laser-induced decoherence on the ^{13}C nuclear spin, we examine a scenario with a continuous readout laser pulse at c_2 during the interpulse spacing τ of a CPMG-1 measurement in $|\downarrow_e\rangle$ shown in Fig. S.7 (e). We observe a reduce of the coherence time T_2 by a factor of 9 from $T^{\mathrm{CPMG1}}_{2,\mathrm{rf1}} = (270 \pm 11)\,\mathrm{ms}$ to $\tilde{T}^{\mathrm{L}}_{2,\mathrm{rf1}} = (30 \pm 6)\,\mathrm{ms}$ [Fig. S.7 (f)]. While the readout laser c_2 is not in resonance with the electron spin manifold $|\downarrow_e\rangle$, residual overlap in the optical transition creates a small probability of exciting the electron spin, potentially leading to a spin flip. Such an uncontrolled flip of the electron spin causes the ^{13}C nuclear spin to decohere, which is especially significant for our strong hyperfine interaction. Recent studies on hyperfine interactions in the excited state [11] indicate that any phase acquired is linear with time spent in the excited state, which can be compensated already by simple decoupling sequences as the Hahn echo or CPMG N=1. However, due to our strong hyperfine coupling it is unclear whether this phase remains linear for our system.

Assuming e.g. that the electron spin is in the state off-resonant to the laser pulse, with a readout window of 660 µs (1/e of laser pulse duration) we would be able to readout the electron spin 45 times before the nuclear spin loses its coherence.

NUMERICAL SIMULATION AND ESTIMATION OF THE MEMORY TIME LIMIT

In order to characterize the performance of our dynamical decoupling sequences in Fig. 3 in the main text for extending the coherence time of the ^{13}C nuclear spin, we consider a simplified model of a two-state quantum system, which is subject to magnetic noise. In addition, we model the power fluctuations of the driving fields and simulate the system evolution numerically. The model is similar to the one used for modeling decoherence of color centers in diamond [2]. We consider the Hamiltonian

$$H(t) = (\omega_0 + \delta(t))\, S_z + 2\Omega_{\mathrm{rf}} f(t)(1 + \epsilon(t)) \cos\left[\omega_0 t + \phi(t)\right] S_x, \qquad (3)$$

where ω_0 is the expected Larmor frequency of the ^{13}C nuclear spin, Ω_{rf} is the peak Rabi frequency of the radio-

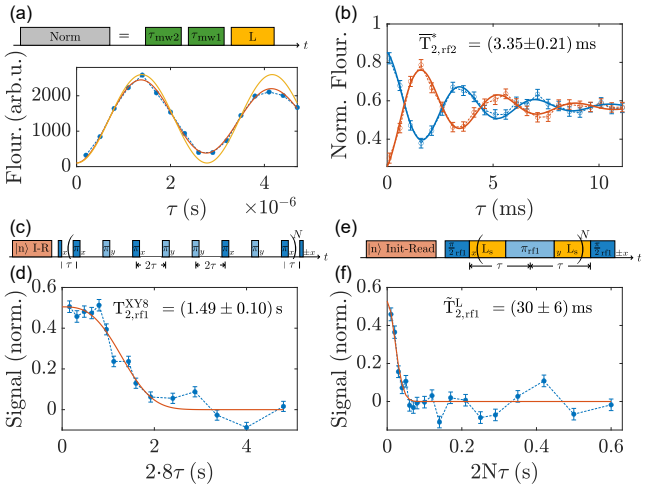

FIG. S.7. (a) Top: Rabi sequence used for normalization that is appended after each measurement. Bottom: Exemplary normalization Rabi for the nuclear XY8 measurement shown in (d). Respective counts are normalized on the maximum and minimum of the non-decayed fit (yellow). (b) Nuclear Ramsey in the $|\uparrow_e\rangle$ state showing a $T^*_{2,\mathrm{rf2}} = (3.35 \pm 0.21)$ ms. (c) XY8 pulse sequence. (d) Nuclear XY8 measurement in $|\downarrow_e\rangle$ yields a $T^{\mathrm{XY8}}_{2,\mathrm{rf1}} = (1.49 \pm 0.10)$ s. (e) CPMG sequence with laser applied during interpulse spacing τ. (f) Nuclear CPMG N=1 with the pulse sequence from (e). We observe reduced T_2 from $T^{\mathrm{CPMG1}}_{2,\mathrm{rf1}} = (270 \pm 11)$ ms to $\tilde{T}^{\mathrm{L}}_{2,\mathrm{rf1}} = (30 \pm 6)$ ms.

frequency (rf) driving field, $f(t)$ characterizes target variation of the Rabi frequency in time, e.g., it can be a step function taking values 0 and 1, while $\phi(t)$ is the phase of the applied field, $S_j = \hbar\sigma_i/2$ with $j \in \{x, y, z\}$ are the respective spin-1/2 operators. The parameters $\delta(t)$ and $\epsilon(t)$ characterize the time-varying errors in the Larmor frequency of the the ^{13}C nuclear spin and the target Rabi frequency.

We move to the interaction picture with respect to $H_0^{(1)} = \omega_0 S_z$ and obtain after applying the rotating-wave approximation ($\Omega_{\mathrm{rf}} \ll \omega_0$)

$$H_1(t) = \delta(t)S_z + \Omega_{\mathrm{rf}} f(t)(1+\epsilon(t))(\cos(\phi(t))S_x + \sin(\phi(t))S_y). \tag{4}$$

We consider this Hamiltonian in the simulation as the rotating-wave approximation is satisfied very well for our experimental parameters.

The noise of the detuning $\delta(t)$ is modelled as an Ornstein-Uhlenbeck (OU) process [12, 13] with a zero expectation value $\langle\delta(t)\rangle = 0$, correlation function $\langle\delta(t)\delta(t')\rangle = \sigma_\delta^2 \exp\{(-|t-t'|/\tau_c)\}$, where $\sigma_\delta^2 = \langle\delta(t)^2\rangle$ is the variance of the detuning due to noise, which is characterized by the standard deviation $\sigma_\delta = \sqrt{D\tau_c/2}$ with D a diffusion constant, and τ_c is the correlation time of the noise for the OU process [13]. More details about the simulation implementation can be found in [2].

We calibrate the effect of environmental noise from the decay time $T_2^* \approx 2$ ms of the signal from a Ramsey measurement (see Fig. 2 (d) in the main text), the decay time $T_2^H \approx 274$ ms of a Hahn echo measurement, where a π pulse is applied in the middle of the interaction (see Fig. 2 (e) in the main text), and the decay times of the CPMG sequences in Fig. 3 in the main text. We note that our spin echo measurement consists of a single block with a duration $\widetilde{\tau} = 2\tau$, which includes the refocusing π pulse. In the following we use $\widetilde{\tau} = 2\tau$ correspond to the typical pulse separation, used for the dynamical decoupling sequences we use. We then obtain the correlation time τ_c by fitting the exact analytical formula for the expected coherence decay rate $\gamma(N, \widetilde{\tau})$ due to magnetic noise (the signal $\sim \exp\{-\gamma(N, \widetilde{\tau})\}$), modelled with an OU process, during a sequence of N ideal, instantaneous π pulses for total evolution time $t = N\widetilde{\tau} = 2N\tau$ [2, 14]:

$$\gamma(N,\widetilde{\tau}) = \sigma_\delta^2\tau_c^2\left[-\left((-1)^{N+1}e^{-\frac{t}{\tau_c}}+1\right)\left(1-\mathrm{sech}\left(\frac{\widetilde{\tau}}{2\tau_c}\right)\right)^2 + t\left(\frac{1}{\tau_c} - \frac{2\tanh\left(\frac{\widetilde{\tau}}{2\tau_c}\right)}{\widetilde{\tau}}\right)\right]. \tag{5}$$

In the usual case when the noise correlation time is much longer than the pulse separation $\tau_c \gg \tau$, as is the case in our experiment, the decay rate simplifies to

$$\gamma_{\mathrm{approx}}(N,\widetilde{\tau}) \approx \sigma_\delta^2 \frac{N\widetilde{\tau}^3}{12\tau_c}. \tag{6}$$

In an experiment where we fix the number of π pulses N and vary the pulse separation time $\widetilde{\tau}$ (as in the experiments in Fig. 3 in the main text), the decay rate as a function of the evolution time t is given by

$$\gamma_{\mathrm{approx}}(N,t) \approx \sigma_\delta^2 \frac{t^3}{12N^2\tau_c}, \tag{7}$$

where we replaced $\widetilde{\tau} = t/N$ in the formula of Eq. (6). We determine the theoretical coherence times $T_2(N)$ for the different orders of the CPMG sequences by solving for $\gamma_{\mathrm{approx}}(N, T_2) = 1$, which leads to

$$T_2(N) \approx \left(\frac{12N^2\tau_c}{\sigma_\delta^2}\right)^{1/3} = T_2^H N^{2/3}, \tag{8}$$

where $T_2^H = \left(\frac{12\tau_c}{\sigma_\delta^2}\right)^{1/3}$ the decay time of a Hahn echo experiment. The dependence of the coherence times $\sim N^{2/3}$ has been experimentally demonstrated in color centers in diamond [15].

Figure S.8(a) shows the estimated correlation time for

different CPMG sequences vs. the number N of the π pulses in the sequence. We fit the decay rate function in Eq. (5) to the experimental data, using NonLinearModelFit procedure in Mathematica. The correlation time estimates vary between 829 ± 197 s for $N = 1$ (Hahn echo) and 2854 ± 929 s for ($N = 2$). The estimates are within the error range, which is the 95% confidence interval for all estimates, except for $N = 1$. The slightly lower value for Hahn echo is most likely due to pulse errors, which are typically well compensated for the CPMG sequences for the particular initial state after the first $\pi/2$ pulse. Figure S.8(b) shows that the coherence times follow the expected $N^{2/3}$ behavior within the error range of the estimated correlation times. Finally, we note that in order to be conservative in our estimation of the theoretical estimation of the memory time limit in the main text (Fig. 3(d)), we use the lower bound of the correlation time estimate, i.e. $\tau_c = 829$ s in all theoretical calculations and simulations.

Quantum memory experiments typically use fixed, optimized pulse separation time $\widetilde{\tau}$ and vary the number N of the applied π pulses. Then, the signal decay rate depends mainly on $\widetilde{\tau}$ and is given by

$$\gamma_{\text{approx}}(\widetilde{\tau}, t) \approx \sigma_\delta^2 \frac{\widetilde{\tau}^2}{12\tau_c} t, \tag{9}$$

where we replaced $N = t/\widetilde{\tau}$ in the formula of Eq. (6). We determine the theoretical memory times $T_2^{\text{mem}}(\widetilde{\tau})$ for the different pulse separation times of the CPMG sequences by solving for $\gamma_{\text{approx}}(\widetilde{\tau}, T_2) = 1$, which leads to

$$T_2^{\text{mem}}(\widetilde{\tau}) \approx \frac{12\tau_c}{\sigma_\delta^2 \widetilde{\tau}^2} = \left(\frac{T_2^H}{\widetilde{\tau}}\right)^2 T_2^H. \tag{10}$$

This is the formula we use in the main text to estimate the maximum achievable memory time, using dynamical decoupling with ideal, instantaneous π pulses. It is evident that, assuming ideal, instantaneous pulses and no detrimental heating effect, reducing the pulse separation time $\widetilde{\tau}$ increases significantly the achievable memory time. We note that reducing the pulse separation time (increasing the number of π pulses) is likely to reach a limit when we take pulse errors into account, so we analyze this next by simulating the process numerically.

Apart from the theoretical limit for the OU noise model, we also simulate the effect that the π pulses are not instantaneous and there are also pulse errors due to detuning and amplitude noise. We described the characteristics of detuning noise above. We model the fluctuations in the driving field amplitude similarly to previous experiments as they typically depend on the used arbitrary waveform generator and amplifier [2, 16, 17]. Specifically, we model the relative error of the Rabi frequency with an OU process with the update function [2, 16]

$$\epsilon(t + \Delta t) = \epsilon(t) e^{-\frac{\Delta t}{\tau_\Omega}} + \widetilde{n_\epsilon} \sqrt{\sigma_\epsilon^2 \left(1 - e^{-\frac{2\Delta t}{\tau_\Omega}}\right)}, \tag{11}$$

where $\sigma_\epsilon = \sqrt{(1/2) D_\Omega \tau_\Omega} = 0.005$, the correlation time $\tau_\Omega = 500\mu$s with the corresponding diffusion constant $D_\Omega = 2\sigma_\epsilon^2/\tau_\Omega$ [18]. The initial values of $\delta(t = 0)$ and $\epsilon(t = 0)$ change from run to run and are taken from a Gaussian distribution with standard deviations σ_δ and σ_ϵ, respectively. The results are demonstrated in the inset of Fig. 3 (b) in the main text. Theoretically, one expects a prolongation of the memory time with shorter pulse separation when the pulses are ideal and instantaneous, which is shown by the solid red line within the Figure. We show that when the pulses are not instantaneous, pulse errors become an important factor when the pulse separation is of the order of 20 ms or shorter. The best possible memory time is then achieved at pulse separation $\widetilde{\tau} = 2\tau \approx 10$ ms. Longer pulse separation does not allow for efficient decoherence suppression for our current noise spectrum while shorter pulse spacing requires many pulses and the performance suffers from pulse errors. Our current experimental setup shows no noticeable heating effect for pulse separation of 24 ms or higher (c.f. subsequent section), so reaching pulse distance of 10 ms might be feasible with modest modifications.

Finally, the achievable memory times are also affected by $T_{1,e}$ relaxation. The memory time limit $T_{2,\text{total}}^{\text{mem}}$ that takes $T_{1,e}$ into account is then determined by the formula

$$\frac{1}{T_{2,\text{total}}^{\text{mem}}(\widetilde{\tau})} = \frac{1}{2T_{1,e}} + \frac{1}{T_2^{\text{mem}}(\widetilde{\tau})}, \tag{12}$$

which we use in Fig. 3 (b) inset in the main text. We show that for pulse separation of the order of 40 ms or shorter, the main memory decay factor is $T_{1,e}$ relaxation. We estimate a memory time of $T_2^{\text{mem}} = 18.1$ s with pulse separation of 24 ms, which is feasible in our experiment without excessive heating. Reducing pulse separation to around 10 ms by improved mw and rf delivery should boost the memory time to $T_2^{\text{mem}} \approx 28$ s where pulse errors with the XY8 sequence start to play a role due to the large number of pulses. Application of higher order sequences like KDD or the UR family [19–21] can in principle boost the memory time limit even closer to the $T_{1,e}$ limit of ≈ 41.4 s.

In the following, we characterize the fidelities of the radio-frequency pulses, which are used in Fig. 3 in the main text. In order to do this we define their fidelity similarly to [2, 19, 20] as

$$F(t) = \frac{1}{2} \left| \text{Tr}\left(U_{1,\text{no noise}}^\dagger(t,0) U_1(t,0) \right) \right|, \tag{13}$$

where $U_{1,\text{no noise}}(t,0) = \exp(-iH_1 t), \delta(t) = 0, \epsilon(t) = 0$ is the target propagator of the pulse without noise and $U_1(t,0) = \exp(-iH_1 t), \delta(t) \neq 0, \epsilon(t) \neq 0$ is the actual one. As the correlation time of the noise is much longer than the duration of the $\pi/2$ and π pulses, we assume for simplicity that the frequency and amplitude noise terms $\delta(t)$ and $\epsilon(t)$ are constant during the interaction. We note that, similarly to Fig. 3 in the main text, we also assume that the nuclear spin measurements are conducted in the

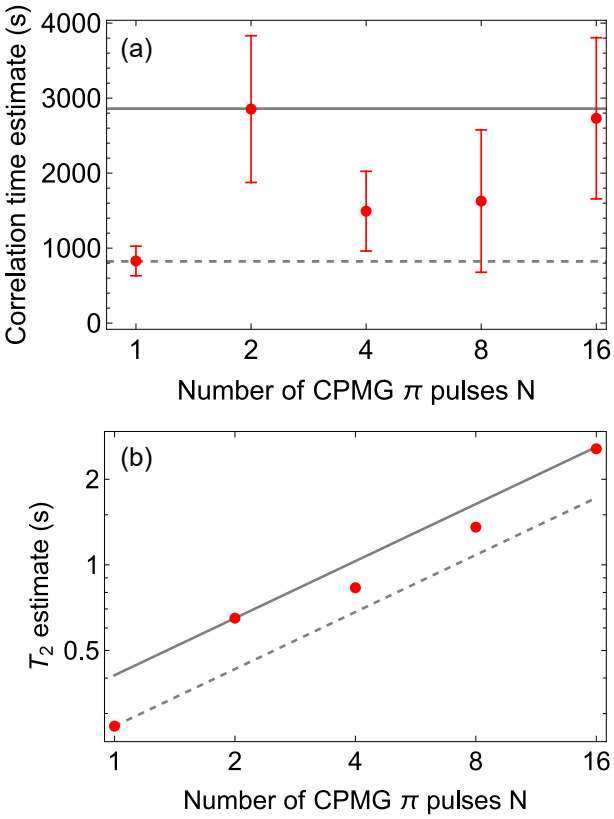

FIG. S.8. (a) Estimated correlation time τ_c of the OU model decay rate for different CPMG sequences vs. the number N of the π pulses in the sequence with $N = 1$, corresponding to the standard Hahn echo (see also Fig. 3 in the main text). (b) Experimentally measured T_2 times of the CPMG sequences vs. the number N of the π pulses in the sequence. The dashed (solid) lines are estimated with the formula in Eq. (8) correspond to the expected minimum (maximum) values from the OU model, given the respective estimates for the correlation time τ_c in (a), showing the expected $N^{2/3}$ dependence, within the respective error range.

$|\downarrow_e\rangle$ manifold, i.e., the electron spin is initialized and remains in state $|\downarrow_e\rangle$ during the experiments.

Figure S.9 shows a simulation of the fidelity of each of the pulses and sequences vs. amplitude and detuning errors. The results show that the fidelities of the $\pi/2$ and π pulses are quite high (Fig. S.9a,b). Specifically, the respective fidelities for detuning and amplitude errors at three standard deviations $\delta = 3\sigma_\delta$ and $\epsilon = 3\sigma_\epsilon$ are $F_{\pi/2} \approx 0.9997$ and $F_\pi \approx 0.9993$. However, the errors accumulate for CPMG, e.g., when it is repeated and consists of eight π pulses (Fig. S.9c), with the corresponding fidelity at three times the standard deviations for eight π pulses with a 10 ms pulse separation equal to $F_{\mathrm{CPMG}} \approx 0.96$. On the contrary, the errors are compensated very well for XY8 for the same number of pulses (Fig. S.9d), with fidelity practically not differing from 1, demonstrating its robustness. We note that all simulations above assume that the the electron spin is initialized and remains in state $|\downarrow_e\rangle$, i.e., these are the fidelitities of the pulses on the rf1 transition.

We obtain very similar fidelities when the electron spin is initialized and remains in state $|\uparrow_e\rangle$, i.e., for radio-frequency pulses on the rf2 transition. These are $F_{\pi/2} \approx 0.9998$ and $F_\pi \approx 0.9994$ where the effect of the slightly lower Rabi frequency of $\Omega_{\mathrm{rf2}} = (2\pi)(7.73 \pm 0.05)\,\mathrm{kHz}$ is compensated by the longer $T^*_{2,\mathrm{rf2}} = (3.35 \pm 0.21)\,\mathrm{ms}$ on the rf2 transition qubit. We note that the eigenstates of the rf2 qubit are superpositions of the bare nuclear spin eigenstates due to the strong A_{zx} coupling, which is a particularity of the specific ^{13}C nuclear spin in the experiment. Finally, driving of the nuclear spin, which is independent of the electron spin state can in principle be achieved by simultaneous driving of the rf1 and rf2 transitions, similarly to experiments with NV centers [22] or as recently demonstrated for the SnV [11].

Heating estimation

In our system, we attribute the primary source of heating to ohmic losses caused by impedance mismatches in the mw/rf delivery, particularly at self-soldered connection points near the sample. Although the wire has minimal contact with the diamond, it is positioned to touch the surface to place the microwave field as close as possible to the color center, which could still transfer some heat to the sample. However, we believe the heat load is mainly transferred via the shared thermal ground at the mixing chamber (MXC) flange, where both the sample (via the cold finger) and the mw/rf supply (via connectors) are connected. Therefore, in our heating estimations, we focus on the heat load generated by the pulse sequences, specifically the number of rf pulses over a given period.

For the possible pulse spacing between π rf pulses we conservatively estimate $\tilde{\tau} = 2\tau = 24\,\mathrm{ms}$ or longer. As the temperature sensor states only a low and delayed rise of temperature for our applied sequences, we choose an alternative approach to estimate the heat load in our system. For this we compare in Fig. S.10 two nuclear Rabi experiments (pulse sequence in Fig. 2 (c) in the main text) and their corresponding electron Rabi normalization curves. In order to be able to compare these results in terms of heating with each other, the measurements were taken on the same day with the same parameters, only differing in duty cycles. We calculate the duty cycle as the ratio of the number of π rf pulses to the total duration of the sequence. For the number of π rf pulses we divide the overall duration of applied rf pulses with the 42.5 µs length of the π rf pulse. For the duration of the sequence we take the substantial elements, i.e. waiting and laser elements, into account. We estimate for the measurement showing no significance of heating a duty cycle of 4.17 %. In the presence of significant heating, we loose contrast in the nuclear Rabi curve (red fit in Fig. S.10 (a)). Moreover, the corresponding electron Rabi

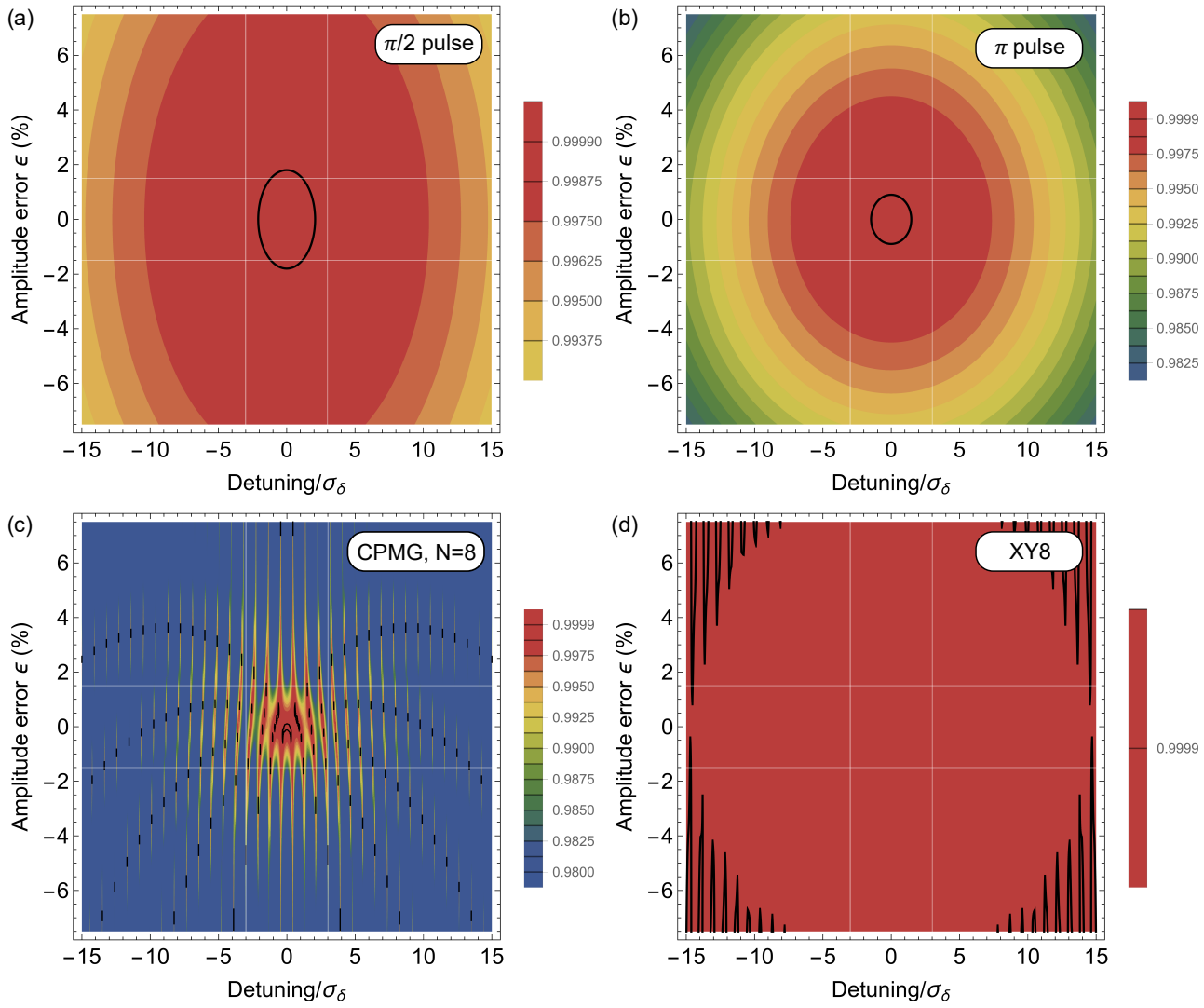

FIG. S.9. Simulation of fidelity of the radio-frequency pulses on the rf1 transition vs. amplitude and detuning errors for (a) a $\pi/2$, (b) a π pulse, (c) the CPMG sequence, repeated to include a total of $N = 8$ pulses, (d) the XY8 sequence. The time separation between the centers of the π pulses of the CPMG and XY8 sequence is 10 ms, corresponding to the optimum time separation from the simulation in Fig. 3 in the main text. The black lines indicate the typical quantum information threshold of $F(t) = 0.9999$. The white lines indicate the range of ± 3 times the standard deviations of the amplitude ($\sigma_\epsilon = 0.005 = 0.5\%$) and frequency detuning ($\sigma_\delta \approx \sqrt{2}/T^*_{2,\mathrm{rf1}} \approx (2\pi)112.5\,\mathrm{Hz}$), used in the simulations. The target Rabi frequency in the simulation is $\Omega(t) = (2\pi)11.73$ kHz. It is evident that XY8 compensates the expected errors very well. All simulations assume that the electron spin is initialized and remains in state $|\downarrow_e\rangle$.

normalization (Fig. S.10 (b)) shows detuned driving with a stronger decay. We estimate for this measurement a duty cycle of 5.38%. The duty cycles correspond to a (not) possible pulse spacing $\widetilde{\tau}$ for the memory estimation of approximately $(1\,\frac{\pi_{\mathrm{rf}}\text{-pulse}}{18.6\,\mathrm{ms}})\ 1\,\frac{\pi_{\mathrm{rf}}\text{-pulse}}{24.0\,\mathrm{ms}}$. The corresponding measured temperatures are 88.5 mK and 93.8 mK, respectively, compared to a base temperature of approximately 77 mK taken by a nearby temperature sensor for a rf input power of 5 W feeded into the cryostat.

[1] Y. N. Palyanov, I. N. Kupriyanov, Y. M. Borzdov, and N. V. Surovtsev, "Germanium: a new catalyst for diamond synthesis and a new optically active impurity in diamond," Scientific reports, vol. 5, no. 1, p. 14789, 2015.
[2] K. Senkalla, G. Genov, M. H. Metsch, P. Siyushev, and F. Jelezko, "Germanium vacancy in diamond quantum memory exceeding 20 ms," Phys. Rev. Lett., vol. 132, p. 026901, Jan 2024.
[3] M. A. Nielsen and I. L. Chuang, Quantum computation and quantum information. Cambridge university press, 2010.

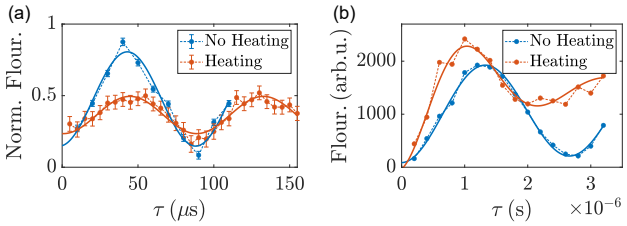

FIG. S.10. (a) Heating estimation using two nuclear Rabi experiments performed on the same day. The contrast in the nuclear Rabi measurements diminishes when substantial heating is present. For the measurement showing no noticeable heating we deduce a possible pulse spacing of $\widetilde{\tau} = 24\,\mathrm{ms}$ feasible for dynamical decoupling sequences. This value is taken for the estimation of an realistic achievable ^{13}C memory time. (b) The corresponding Rabi normalization shows a detuned driving for the case of significant heating.

[4] G. Thiering and A. Gali, "Ab Initio magneto-optical spectrum of group-IV vacancy color centers in diamond," Phys. Rev. X, vol. 8, p. 021063, Jun 2018.

[5] R. Storn and K. Price, "Differential evolution–a simple and efficient heuristic for global optimization over continuous spaces," Journal of global optimization, vol. 11, pp. 341–359, 1997.

[6] A. Schweiger and G. Jeschke, Principles of pulse electron paramagnetic resonance. Oxford University Press, 2001.

[7] J. F. Barry, J. M. Schloss, E. Bauch, M. J. Turner, C. A. Hart, L. M. Pham, and R. L. Walsworth, "Sensitivity optimization for NV-diamond magnetometry," Rev. Mod. Phys., vol. 92, p. 015004, Mar 2020.

[8] M. Rossignolo, T. Reisser, A. Marshall, P. Rembold, A. Pagano, P. J. Vetter, R. S. Said, M. M. Müller, F. Motzoi, T. Calarco, F. Jelezko, and S. Montangero, "QuOCS: The quantum optimal control suite," Computer Physics Communications, vol. 291, p. 108782, 2023.

[9] N. Rach, M. M. Müller, T. Calarco, and S. Montangero, "Dressing the chopped-random-basis optimization: A bandwidth-limited access to the trap-free landscape," Phys. Rev. A, vol. 92, p. 062343, Dec 2015.

[10] M. M. Müller, R. S. Said, F. Jelezko, T. Calarco, and S. Montangero, "One decade of quantum optimal control in the chopped random basis," Reports on progress in physics, vol. 85, no. 7, p. 076001, 2022.

[11] H. K. Beukers, C. Waas, M. Pasini, H. B. van Ommen, N. Codreanu, J. M. Brevoord, T. Turan, M. Iuliano, Z. Ademi, T. H. Taminiau, et al., "Control of solid-state nuclear spin qubits using an electron spin-1/2," arXiv preprint arXiv:2409.08977, 2024.

[12] M. C. Wang and G. E. Uhlenbeck, "On the theory of the Brownian motion II," Rev. Mod. Phys., vol. 17, pp. 323–342, Apr 1945.

[13] D. T. Gillespie, "The mathematics of Brownian motion and Johnson noise," American Journal of Physics, vol. 64, no. 3, pp. 225–240, 1996.

[14] M. F. Pascual-Winter, R.-C. Tongning, T. Chanelière, and J.-L. Le Gouët, "Spin coherence lifetime extension in Tm^{3+}:YAG through dynamical decoupling," Phys. Rev. B, vol. 86, p. 184301, Nov 2012.

[15] N. Bar-Gill, L. M. Pham, A. Jarmola, D. Budker, and R. L. Walsworth, "Solid-state electronic spin coherence time approaching one second," Nature Communications, vol. 4, pp. 1–6, apr 2013.

[16] G. T. Genov, N. Aharon, F. Jelezko, and A. Retzker, "Mixed dynamical decoupling," Quantum Science and Technology, vol. 4, p. 035010, jul 2019.

[17] G. T. Genov, Y. Ben-Shalom, F. Jelezko, A. Retzker, and N. Bar-Gill, "Efficient and robust signal sensing by sequences of adiabatic chirped pulses," Phys. Rev. Research, vol. 2, p. 033216, Aug 2020.

[18] N. Aharon, I. Cohen, F. Jelezko, and A. Retzker, "Fully robust qubit in atomic and molecular three-level systems," New Journal of Physics, vol. 18, p. 123012, dec 2016.

[19] A. M. Souza, G. A. Álvarez, and D. Suter, "Robust dynamical decoupling," Philosophical Transactions of the Royal Society A: Mathematical, Physical and Engineering Sciences, vol. 370, pp. 4748–4769, 10 2012.

[20] G. T. Genov, D. Schraft, N. V. Vitanov, and T. Halfmann, "Arbitrarily Accurate Pulse Sequences for Robust Dynamical Decoupling," Physical Review Letters, vol. 118, p. 133202, Mar 2017.

[21] N. Ezzell, B. Pokharel, L. Tewala, G. Quiroz, and D. A. Lidar, "Dynamical decoupling for superconducting qubits: A performance survey," Phys. Rev. Appl., vol. 20, p. 064027, Dec 2023.

[22] J. F. Barry, M. H. Steinecker, S. T. Alsid, J. Majumder, L. M. Pham, M. F. O'Keeffe, and D. A. Braje, "Sensitive ac and dc magnetometry with nitrogen-vacancy-center ensembles in diamond," Phys. Rev. Appl., vol. 22, p. 044069, Oct 2024.